

Cross-Domain Waveform Design for 6G Integrated Sensing and Communication

Fan Zhang, *Student Member, IEEE*, Tianqi Mao, *Member, IEEE*, Ruiqi Liu, *Member, IEEE*,
 Zhu Han, *Fellow, IEEE*, Octavia A. Dobre, *Fellow, IEEE*,
 Sheng Chen, *Life Fellow, IEEE*, and Zhaocheng Wang, *Fellow, IEEE*

Abstract—Orthogonal frequency division multiplexing (OFDM) is one of the representative integrated sensing and communication (ISAC) waveforms, where sensing and communications tend to be assigned with different resource elements (REs) due to their diverse design requirements. This motivates optimization of resource allocation/waveform design across time, frequency, power and delay-Doppler domains. Therefore, this article proposes two cross-domain waveform optimization strategies for OFDM-based ISAC systems, following communication-centric and sensing-centric criteria, respectively. For the communication-centric design, to maximize the achievable data rate, a fraction of REs are optimally allocated for communications according to prior knowledge of the communication channel. The remaining REs are then employed for sensing, where the sidelobe level and peak-to-average power ratio are suppressed by optimizing its power-frequency and phase-frequency characteristics. For the sensing-centric design, a ‘locally’ perfect auto-correlation property is ensured by adjusting the unit cells of the ambiguity function within its region of interest (RoI). Afterwards, the irrelevant cells beyond RoI, which can readily determine the sensing power allocation, are optimized with the communication power allocation to enhance the achievable data rate. Numerical results demonstrate the superiority of the proposed communication-centric and sensing-centric waveform designs for ISAC applications.

Index Terms—Integrated sensing and communication (ISAC), sixth-generation (6G), orthogonal frequency division multiplexing (OFDM), cross-domain waveform design, ambiguity function.

I. INTRODUCTION

With the commercialization of the fifth-generation (5G) networks, early explorations of the game-changing sixth-

This work was supported in part by the National Natural Science Foundation of China under Grant U22B2057, in part by Young Elite Scientists Sponsorship Program by CAST under Grant 2022QNRC001, and in part by Postdoctoral Science Foundation of China under Grant 2022M720361 and 2023T160040. Part of this work has been submitted to IEEE WCNC 2024 [1]. (*Corresponding authors: Zhaocheng Wang, Tianqi Mao*)

F. Zhang and Z. Wang are with Beijing National Research Center for Information Science and Technology, Department of Electronic Engineering, Tsinghua University, Beijing 100084, China, and Z. Wang is also with Tsinghua Shenzhen International Graduate School, Shenzhen 518055, China (e-mails: zf22@mails.tsinghua.edu.cn, zcwang@tsinghua.edu.cn).

T. Mao is with the School of Electronic and Information Engineering, Beihang University, Beijing 100191, China (e-mail: maotq@buaa.edu.cn).

R. Liu is with the Wireless and Computing Research Institute, ZTE Corporation, Beijing 100029, China, and also with the State Key Laboratory of Mobile Network and Mobile Multimedia Technology, Shenzhen 518055, China (e-mail: richie.leo@zte.com.cn).

Z. Han is with the Department of Electrical and Computer Engineering, University of Houston, Houston, TX 77004 USA, and also with the Department of Computer Science and Engineering, Kyung Hee University, Seoul 446-701, South Korea (e-mail: hanzhu22@gmail.com).

O. A. Dobre is with the Faculty of Engineering and Applied Science, Memorial University, St. John’s, NL A1C 5S7, Canada (e-mail: odobre@mun.ca).

S. Chen is with the School of Electronics and Computer Science, University of Southampton, Southampton SO17 1BJ, U.K. (e-mail: sqc@ecs.soton.ac.uk).

generation (6G) concept have been initiated by a collection of countries, being envisioned to support unprecedented ubiquitous communications and sensing [2]–[5]. Promoted by the ever-progressing digital signal processing techniques, the transceiver structure for data transmission and radar sensing has become increasingly correlated [6]–[8]. This facilitates the convergence of sensing and communications by sharing identical hardware and spectrum resources, yielding the integrated sensing and communication (ISAC) philosophy [9]–[14]. Such cutting-edge technology can realize both functions simultaneously with reasonable hardware expense and efficient bandwidth/energy usage, which supports a plethora of emerging applications, e.g., autonomous driving, smart home, extended reality (XR), airborne reconnaissance/monitoring, etc. [10]–[12]. Thanks to these merits, ISAC has attracted extensive attentions as a promising enabling technology for 6G networks and is recognized as one of six independent usage scenarios of 6G [15]–[17].

Existing literature has reached a consensus that the broad-sense concept of ISAC can be classified into three categories: co-existence, cooperation and co-design [18], [19]. Co-existing radar and communication subsystems are mutually treated as independent and adverse interferers, whilst the cooperation counterpart can mitigate the interference through information exchange. However, these two approaches do not fully integrate communication and sensing subsystems, which induces additional hardware expenses and computational complexity for interference management. Alternatively, the co-design philosophy shares unitary hardware platform and transmit waveform for simultaneous sensing and communications, which reaches true harmony across space, time and spectrum domains. Therefore, this article is concentrated on the co-design methodologies of ISAC¹.

A. Related Works

An appropriate dual-functional waveform design is crucial for ISAC systems [20], which is challenging due to the diverse requirements of communication and sensing functions. Specifically, communication systems tend to employ stochastic signals with superior spectral/energy efficiency, whilst sequences with good auto-correlation property are preferable for sensing applications. To accommodate these very different specifications, one promising representative is orthogonal frequency division multiplexing (OFDM) [20]–[22], which is widely adopted in current communication standards like the fourth-generation

¹In the following, we refer to “ISAC” as the co-design methodology for communication and radar convergence.

(4G) Long-Term Evolution LTE [23] and 5G new radio (NR) [24] thanks to the merits of OFDM signals like robustness to frequency-selective fading and easy implementation. Despite of its randomness, the OFDM waveform possesses perfect auto-correlation property when using constant-amplitude constellations, e.g., phase-shift keying (PSK) [25]. Under such a waveform design, OFDM can readily support accurate sensing with marginal modifications to the existing infrastructure [26]. However, such an ideal auto-correlation property is no longer guaranteed when the quadrature amplitude modulation (QAM) format is employed for higher spectral efficiency [25], [27]. Moreover, for the application scenario which performs sensing in a broadcasting/scanning mode, whilst providing directional access to user terminals simultaneously [28], [29], the communication and sensing components should be non-overlapped in the time-frequency domain to avoid possible interference.

To tackle the aforementioned issues, an integrated OFDM waveform design with interleaved subcarriers, abbreviated as OFDM-IS, was explored in the existing literature, where the dual functions are allocated with orthogonal spectrum resources [30]–[35]. Specifically, in [30], the assignment and power allocation of OFDM subcarriers were optimized for the communication and sensing subsystems using a compound mutual-information (MI) based objective function, where both a radar-selfish and a balanced design strategies were developed. Another joint subcarrier and power allocation optimization strategy was proposed in [31] and [32], aiming to minimize the total power consumption under constraints on the MI metric for radar sensing and the data rate for communication. The work [33] further proposed a robust multi-carrier waveform design against imperfect channel state information, where the bit and power allocation strategies were optimized with a greedy algorithm.

Rather than adopting the MI-related metrics for radar sensing, the study [34] optimized the joint subcarrier and power allocation strategy between the dual functions by maximizing the peak-to-sidelobe ratio (PSLR) in the radar range profile², whilst ensuring an acceptable level of the communication data rate. Unlike the aforementioned works which merely focused on the frequency- and power-domain characteristics, in [35], the optimum OFDM-IS design for ISAC applications was cleverly extended to the time domain by involving multiple consecutive OFDM symbols, and multiple resource element (RE) assignment strategies were proposed. These strategies can achieve large time-frequency aperture with a tiny fraction of OFDM resources, whose optimality, however, was not validated with sufficient theoretical derivations. Also the authors of [35] placed emphasis on maximization of the radar aperture, whilst the communication performance of the ISAC waveform cannot be guaranteed.

B. Motivation and Our Contributions

From the above discussions, most of the existing literature on OFDM-IS-based ISAC waveform design only consider

²The radar range profile is referred to as a one-dimensional correlation function of the sensing sequence.

subcarrier assignment and power allocation within a single OFDM symbol. In order to improve the speed resolution in radar sensing, however, the coherent processing interval usually have to be extended by incorporating multiple consecutive OFDM symbols [6]. Considering the time-varying characteristics of the channel in high-speed scenarios, e.g., autonomous driving, it is difficult to apply the resource allocation strategy within one single OFDM symbol to the extended time interval. Consequently, to ensure a more balanced trade-off between sensing and communications across relatively long time intervals, optimization of the ISAC waveform design across multiple consecutive OFDM symbols is necessary, where the existing attempts are still at their infancy. To the authors' best knowledge, the work [35] is the only existing reference involving multiple consecutive OFDM symbols in RE and subcarrier assignment but the design of [35] suffers from some drawbacks as discussed above. Against this background, we propose a cross-domain ISAC waveform design based on the OFDM-IS structure. The waveform coefficients are optimized across time, frequency, power and even delay-Doppler domains, where both a communication-centric and sensing-centric design methodologies are developed, respectively. The main contributions of this paper can be summarized as follows.

- 1) *Communication-centric waveform design:* For maximization of the achievable data rate, a fraction of REs within each frame of multiple consecutive OFDM symbols are optimally assigned for communications through a water-filling algorithm based on prior knowledge of the time-frequency doubly-dispersive channel. The radar sensing components are then constituted by the concatenation of the remaining REs, where the energy budget is optimized in a subcarrier-wise manner to guarantee high PSLR of the radar ambiguity function. The phase-frequency characteristic of the sensing component is further adjusted based on the branch-and-bound (BB) algorithm for the peak-to-average power ratio (PAPR) reduction.
- 2) *Sensing-centric waveform design:* To ensure superior target sensing performance, we firstly construct a ‘locally’ perfect auto-correlation property by shaping the radar ambiguity function of the integrated waveform within a pre-defined region of interest (RoI) in the delay-Doppler domain. Next we approximate Hermitian symmetry for the 2-dimensional ambiguity function. The unit cells of the ambiguity function beyond RoI, referred to as ‘irrelevant cells’ for brevity, can then be directly manipulated to determine the power allocation pattern for sensing, where the REs with relatively low sensing power are employed for data transmission with water filling. Therein the irrelevant cells and the power allocation strategy for communications are jointly optimized for throughput enhancement in an alternating iterative manner.
- 3) Numerical results are provided to validate the superiority of the proposed communication-centric and sensing-centric waveform designs. The proposed communication-centric waveform is capable of achieving a high PSLR within RoI and a low PAPR while maintaining the

optimal achievable data rate, compared with its classical counterparts. On the other hand, while ensuring a locally perfect auto-correlation property, the proposed sensing-centric waveform can approximate the maximum achievable data rate, demonstrating the feasibility of the proposed alternating iterative algorithm. Moreover, the effects of the key parameters on sensing and communication performance are investigated, to provide valuable guidance for the implementation of the proposed sensing-centric waveform design.

C. Structure and Notations

The remainder of this paper is organized as follows. Section II introduces the ODFM-IS-based ISAC system model. Section III defines the RoI in the ambiguity function and presents the proposed communication-centric waveform design. In Section IV, the sensing-centric waveform design is formulated as an optimization problem and an alternating iterative algorithm is developed to solve the problem. Numerical results are provided in Section V, which is followed by conclusions in Section VI.

In this paper, $DFT(\mathbf{X}, 1)$ and $DFT(\mathbf{X}, 2)$ denote performing discrete Fourier transformation (DFT) on every row and every column of matrix \mathbf{X} , respectively. $IDFT(\mathbf{X}, 1)$ and $IDFT(\mathbf{X}, 2)$ denote performing inverse DFT (IDFT) on every row and every column of \mathbf{X} , respectively. $(\mathbf{X})^T$ and $(\mathbf{X})^*$ stand for the transpose and conjugate of \mathbf{X} , respectively. $|\mathbf{X}|$ and $\text{angle}(\mathbf{X})$ denote the element-wise amplitude and phase values of \mathbf{X} , respectively. $|\mathbf{X}|^2$ is a matrix that contains the element-wise absolute square values of \mathbf{X} , and $\|\mathbf{X}\|$ denotes the Frobenius norm of \mathbf{X} . $\mathbf{X} \odot \mathbf{Y}$ denotes the Hadamard product of matrices \mathbf{X} and \mathbf{Y} . For a two-dimensional matrix \mathbf{X} , $X(m, k)$ denotes the element in the m -th row and the k -th column of \mathbf{X} . $\mathbf{1}$ denotes the all-one matrix. $x \sim \mathcal{CN}(0, \sigma^2)$ represents the random variable x that follows a complex Gaussian distribution with mean 0 and variance σ^2 . $\lfloor \cdot \rfloor$ is the floor operation that rounds a real number to the nearest integer less than or equal to the number. $\text{card}(\mathcal{N})$ denotes the cardinality of set \mathcal{N} .

II. ISAC SYSTEM

We consider a monostatic ISAC system as illustrated in Fig. 1, where a base station (BS) sends data to a user equipment (UE).

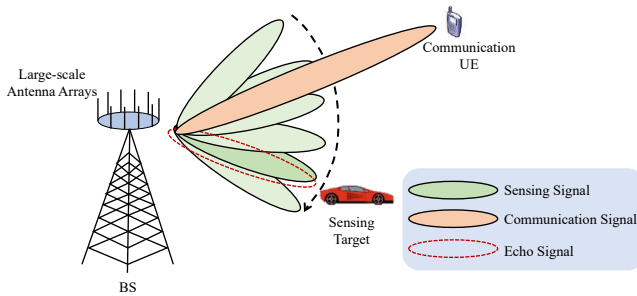


Fig. 1. Typical ISAC scenario with large-scale antenna arrays.

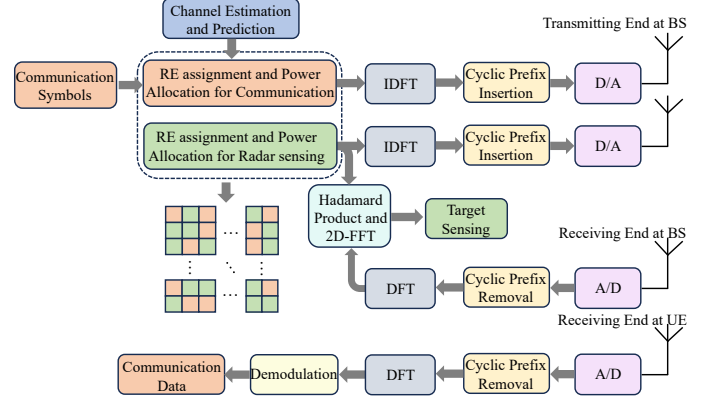


Fig. 2. Transceiver model of the OFDM-IS-based ISAC system.

ment (UE) while simultaneously scanning different directions alternatively for target sensing by emitting radar signals. To guarantee sufficient array gain, large-scale antenna arrays are employed to form highly directional beams for communications and sensing, respectively, especially for millimeter wave frequencies and above. Since the antenna array with directional beamforming is approximately equivalent to a single directional antenna, we consider single-input single-output systems for both communications and sensing for simplicity.

A. Signal Model

The OFDM-IS waveform is employed for target sensing and data transmission, and the corresponding transceiver model is depicted in Fig. 2. Specifically, a frame of M consecutive OFDM symbols with N_c subcarriers is considered for each coherent processing interval and the k -th subcarrier of the m -th symbol is called the (m, k) -th RE. To avoid mutual interference between the sensing and communication, these two subsystems occupy different REs in each frame [30], [32], [34]. For clarity we employ the matrix $\mathbf{U} \in \mathbb{Z}^{M \times N_c}$ to indicate whether REs are selected for sensing or communication purpose

$$U(m, k) = \begin{cases} 1, & \text{the } (m, k)\text{-th RE is for sensing,} \\ 0, & \text{the } (m, k)\text{-th RE is for communications.} \end{cases} \quad (1)$$

Let $\mathbf{S} \in \mathbb{C}^{M \times N_c}$ denote the transmit signal matrix, where $S(m, k)$ represents the modulated symbol on the (m, k) -th RE. Then, the sensing and communication transmit signal matrices, denoted as $\mathbf{S}_r \in \mathbb{C}^{M \times N_c}$ and $\mathbf{S}_c \in \mathbb{C}^{M \times N_c}$, can be expressed as

$$\mathbf{S}_r = \mathbf{U} \odot \mathbf{S}, \quad (2)$$

$$\mathbf{S}_c = (\mathbf{1} - \mathbf{U}) \odot \mathbf{S}. \quad (3)$$

Define $\mathbf{P}_r \in \mathbb{R}^{M \times N_c}$ and $\mathbf{P}_c \in \mathbb{R}^{M \times N_c}$ as the power allocation matrices for sensing and communications, which can be written as $P_r(m, k) = |S_r(m, k)|^2$ and $P_c(m, k) = |S_c(m, k)|^2$, respectively. By modulating \mathbf{S}_r and \mathbf{S}_c on different REs of the OFDM frame, the time-domain transmit signals, $x_i(t)$, $i \in \{r, c\}$, for sensing and communications, respectively,

can be expressed as

$$x_i(t) = \frac{1}{\sqrt{N_c}} \sum_{m=0}^{M-1} \sum_{k=0}^{N_c-1} S_i(m, k) e^{j2\pi k \Delta f (t - mT)} \text{rect}\left(\frac{t - mT}{T}\right), \quad (4)$$

where Δf is the subcarrier spacing and $T = 1/\Delta f$ is the duration of one OFDM symbol, while $\text{rect}(\cdot)$ is the rectangle function, which is defined by

$$\text{rect}(t) = \begin{cases} 1, & 0 \leq t < 1, \\ 0, & \text{otherwise.} \end{cases} \quad (5)$$

Sampling $x_i(t)$ with the period T/N_c leads to the discrete sequence $\bar{x}_i(n) = x_i(nT/N_c)$ as:

$$\bar{x}_i(n) = \frac{1}{\sqrt{N_c}} \sum_{m=0}^{M-1} \sum_{k=0}^{N_c-1} S_i(m, k) e^{j2\pi \frac{k(n-mN_c)}{N_c}} \text{rect}_m(n), \quad (6)$$

with $n = 0, 1, \dots, MN_c - 1$, where $\text{rect}_m(n) = \text{rect}\left(\frac{n-mN_c}{N_c}\right)$. The cyclic prefix (CP) of length T_G is then inserted to mitigate the inter-frame interference. Therefore, the total duration of one OFDM symbol T_O is $T_O = T + T_G$. Finally, the discrete signals are fed into the digital-to-analog (D/A) converter and transmitted through antennas.

B. Communication Channel Model

The standard multi-path time-varying channel model is considered, which is expressed as

$$h_c(t, f) = \sum_{l=1}^L \alpha_l e^{j2\pi(v_l t - \tau_l f)}, \quad (7)$$

where L is the number of paths, and α_l , τ_l and v_l denote the complex gain, delay and Doppler shift of the l -th path, respectively [36]. For simplicity, we assume that each RE experiences time-invariant flat channel fading [37]. By sampling the channel with the period of T_O in time domain and Δf in frequency domain, the discrete channel matrix $\mathbf{H}_c \in \mathbb{C}^{M \times N_c}$ corresponding to different REs within the OFDM frame can be written as

$$H_c(m, k) = \sum_{l=1}^L \alpha_l e^{j2\pi(v_l m T_O - \tau_l k \Delta f)}, \quad (8)$$

which is assumed to be perfectly estimated and predicted. At the receiving end, after the analog-to-digital (A/D) conversion, CP removal and DFT operation, the received signal matrix $\mathbf{Y}_c \in \mathbb{C}^{M \times N_c}$ is obtained, which can be written as

$$\mathbf{Y}_c = \mathbf{H}_c \odot \mathbf{S}_c + \mathbf{W}_c. \quad (9)$$

Here $\mathbf{W}_c \in \mathbb{C}^{M \times N_c}$ is the matrix representation of the additive white Gaussian noise (AWGN) whose entries follow $W_c(m, k) \sim \mathcal{CN}(0, \sigma_c^2)$. Afterward, the communication data can be extracted from \mathbf{Y}_c by demodulation.

C. Target Sensing

By denoting the distance and radial speed of the target relative to the BS as d and u , respectively, the received echoes

$\bar{y}_r(n)$ of the sensing subsystem can be written as

$$\bar{y}_r(n) = \bar{x}_r\left(n - \left\lfloor \frac{2d}{cT_s} \right\rfloor\right) e^{j\left(2\pi n \frac{2u f_c T_s}{c}\right)} + w_r[n], \quad (10)$$

where f_c and T_s denote the carrier frequency and the sampling period, respectively, while $w_r[n]$ denotes the thermal noise plus the clutters from other directions, which follows a complex Gaussian distribution, i.e., $w_r[n] \sim \mathcal{CN}(0, \sigma_r^2)$. The sensing signal matrix $\mathbf{Y}_r \in \mathbb{C}^{M \times N_c}$ can be derived by the DFT and serial-to-parallel operation on $\bar{y}_r(n)$, and can be expressed as

$$Y_r(m, k) = \sum_{n=(m-1)N_c}^{mN_c-1} \bar{y}_r(n) e^{j2\pi \frac{(n-(m-1)N_c)k}{N_c}}. \quad (11)$$

For sensing purpose, the target range and speed are estimated by calculating the two-dimensional cross-correlation between the transmitted sensing sequence and its echoes. Assuming that the time delay of the target is shorter than T_G , the cross-correlation is equivalent to performing DFT and IDFT on the Hadamard product of $(\mathbf{S}_r)^*$ and \mathbf{Y}_r , which is expressed as

$$\mathbf{E} = \text{DFT}(\text{IDFT}((\mathbf{S}_r)^* \odot \mathbf{Y}_r, 1), 2). \quad (12)$$

Let $\nu = 0, 1, \dots, M-1$ and $\tau = 0, 1, \dots, N_c-1$ denote the indices of \mathbf{E} in the Doppler and time domain, respectively. The target can be detected by the hypothesis tests:

$$H_1 : \frac{|E(\nu, \mu)|^2}{\theta(\nu, \mu)} > \Gamma, \quad H_0 : \frac{|E(\nu, \mu)|^2}{\theta(\nu, \mu)} < \Gamma, \quad (13)$$

where Γ is a predefined test threshold. Hypothesis H_1 represents that the point (ν, μ) corresponds to a true target, and vice versa for hypothesis H_0 . $\theta(\nu, \mu)$ is the average noise power estimation at the point (ν, μ) , which can be calculated by averaging the value of $|E(\nu, \mu)|^2$ [38], [39].

For a given point (ν_0, μ_0) , if hypothesis H_1 holds true, distance d and radial speed u of the corresponding target can be expressed respectively as [6]

$$d = \frac{c\mu_0}{2N_c \Delta f}, \quad \mu_0 = 0, 1, \dots, N_c - 1, \quad (14)$$

$$u = \begin{cases} \frac{c\nu_0}{2M f_c T_O}, & \nu_0 = 0, 1, \dots, \lfloor M/2 \rfloor, \\ -\frac{c(M-\nu_0)}{2M f_c T_O}, & \nu_0 = \lfloor M/2 \rfloor + 1, \dots, M-1, \end{cases} \quad (15)$$

where c is the speed of light. Since the time delay of the target is limited by the CP length, the maximum sensing ranges of distance and speed can be expressed as $[0, \frac{T_G}{2}]$ and $(-\frac{c}{4f_c T_O}, \frac{c}{4f_c T_O})$, respectively. However, in practical applications, such as autonomous driving, the ranges of interest are usually smaller than the maximum sensing ranges. This will be discussed in the next section.

III. COMMUNICATION-CENTRIC ISAC WAVEFORM DESIGN

In this design, a fraction of REs with good channel conditions are firstly assigned for communication to optimize the achievable data rate. Then the sensing energy budget is optimally allocated to the remaining REs to obtain high PSLR of the ambiguity function. Finally, the phases of sensing

symbols are designed for PAPR reduction using the BB algorithm. Before detailing this design, we introduce the ambiguity function of the OFDM-based waveform.

A. Ambiguity Function of OFDM-Based Waveform

The ambiguity function is defined as a two-dimensional correlation function in delay-Doppler domain, which can be categorized into the cross-ambiguity function and the auto-ambiguity function. We focus on the auto-ambiguity function of the sensing sequence, i.e., its auto-correlation property, which reflects its capability of radar sensing. Specifically, the auto-ambiguity function $\chi_a(\nu, \mu)$ of the discrete signal $x(n)$ with length N can be expressed as [36], [38]

$$\chi_a(\nu, \mu) = \sum_{n=0}^{N-1} x(n)x^*(n + \mu)e^{j2\pi\nu n/N}, \quad (16)$$

where μ and ν denote the delay and Doppler indices, respectively. By substituting the OFDM-based sensing sequence (6) into (16), the auto-ambiguity function can be derived as

$$\begin{aligned} \chi_a(\nu, \mu) &= \sum_{n=0}^{MN_c-1} \left(\sum_{m_1=0}^{M-1} \sum_{k_1=0}^{N_c-1} S(m_1, k_1) \psi(n, m_1, k_1) \right) \\ &\quad \times \left(\sum_{m_2=0}^{M-1} \sum_{k_2=0}^{N_c-1} S^*(m_2, k_2) \psi^*(n + \mu, m_2, k_2) \right) e^{j2\pi \frac{\nu n}{MN_c}} \\ &= \sum_{n=0}^{MN_c-1} \left(\sum_{m_1=0}^{M-1} \left(\sum_{m_2=0}^{M-1} \psi(n, m_1, k_1) \psi^*(n + \mu, m_2, k_2) \right) \right. \\ &\quad \times \left. \left(\sum_{k_1=0}^{N_c-1} \sum_{k_2=0}^{N_c-1} S(m_1, k_1) S^*(m_2, k_2) \right) \right) e^{j2\pi \frac{n\nu}{MN_c}}, \end{aligned} \quad (17)$$

where $\psi(n, m, k) = e^{j2\pi k(n - mN_c)/N_c} \text{rect}_m(n)$. Due to the CP protection, the inter-frame ($m_1 \neq m_2$) interference is negligible. Therefore, (17) can be further expressed as

$$\begin{aligned} \chi_a(\nu, \mu) &= \sum_{m=0}^{M-1} \sum_{\bar{n}=0}^{N_c-1} \sum_{k_1=0}^{N_c-1} \sum_{k_2=0}^{N_c-1} \left(e^{j2\pi \frac{(k_1 - k_2)(mN_c + \bar{n}) - k_2 \mu}{N_c}} \times \right. \\ &\quad \left. S(m, k_1) S^*(m, k_2) \right) e^{j2\pi \nu \frac{mN_c + \bar{n}}{MN_c}}, \end{aligned} \quad (18)$$

where $\bar{n} = n - mN_c$. For simplicity, we focus on the auto-correlation component of each subcarrier ($k_1 = k_2$), while neglecting the cross-correlation component between different subcarriers ($k_1 \neq k_2$), since the cross-correlation is marginal due to the subcarrier orthogonality [38]. Therefore, the auto-ambiguity function can be approximated as

$$\chi_a(\nu, \mu) \approx \gamma(\nu, \mu) \cdot \eta(\nu), \quad (19)$$

with

$$\gamma(\nu, \mu) \triangleq \sum_{m=0}^{M-1} \sum_{k=0}^{N_c-1} P(m, k) e^{-j2\pi \mu k / N_c} e^{j2\pi \nu m / M}, \quad (20)$$

$$\eta(\nu) \triangleq \sum_{\bar{n}=0}^{N_c-1} e^{j2\pi \nu \bar{n} / (MN_c)}. \quad (21)$$

Note that only $\gamma(\nu, \mu)$ is related to the waveform design. Since $\gamma(\nu, \mu)$ reaches its maximum when ν and μ are multiples of M and N_c , respectively, we consider the region $(\nu, \mu) \in \Omega = [-\lfloor \frac{M}{2} \rfloor, \dots, -1, 0, 1, \dots, M-1 - \lfloor \frac{M}{2} \rfloor] \times [-\lfloor \frac{N_c}{2} \rfloor, \dots, -1, 0, 1, \dots, N_c-1 - \lfloor \frac{N_c}{2} \rfloor]$ to avoid the ambiguity problem in target detection [40]. As the sensing distance and the speed of interest in practical applications are commonly smaller than the maximum sensing ranges corresponding to region Ω in the ambiguity function, we define the RoI Ω_s in the ambiguity function as

$$\begin{aligned} \Omega_s = & \left[-\left\lfloor \frac{M}{2a} \right\rfloor, \dots, -1, 0, 1, \dots, \frac{M}{a} - 1 - \left\lfloor \frac{M}{2a} \right\rfloor \right] \\ & \times \left[0, 1, 2, \dots, \frac{N_c}{b} - 1 - \left\lfloor \frac{N_c}{2b} \right\rfloor \right]. \end{aligned} \quad (22)$$

Given the required sensing scopes of distance $[0, d_0]$ and speed $[-u_0, u_0]$, a and b are chosen as the largest factors of M and N_c , respectively, such that $(-\frac{c}{4af_c T_O}, \frac{c}{4af_c T_O})$ and $[0, \frac{c}{2b\Delta f})$ contain $[-u_0, u_0]$ and $[0, d_0]$, respectively. That is, for Ω_s of (22), the sensing ranges of distance and speed are $[0, \frac{c}{2a\Delta f})$ and $(-\frac{c}{4bf_c T_O}, \frac{c}{4bf_c T_O})$, respectively. Let $F(\Omega_s)$ be the highest sidelobe in RoI, namely,

$$F(\Omega_s) = \max\{|\chi_a(\nu, \mu)| : (\nu, \mu) \in \Omega_s, (\nu, \mu) \neq (0, 0)\}. \quad (23)$$

The PSLR within Ω_s is $\frac{|\chi_a(0, 0)|}{F(\Omega_s)}$, which is adopted to characterize the sensing performance.

B. Waveform Design Methodology

The communication-centric ISAC waveform design consists of the following three steps.

Step 1. Communication RE and power allocation: Given the total communication power \bar{P}_c and the estimated communication channel $\hat{H}_c \in \mathbb{C}^{M \times N_c}$, the communication power allocation strategy is to maximize the achievable data rate, which is formulated as

$$\begin{aligned} \mathcal{P}1 : \quad & \max_{\mathbf{P}_c} \quad \sum_{m=0}^{M-1} \sum_{k=0}^{N_c-1} \log \left(1 + \frac{P_c(m, k) |\hat{H}_c(m, k)|^2}{\sigma_c^2} \right), \\ & \text{s.t.} \quad \sum_{m=0}^{M-1} \sum_{k=0}^{N_c-1} P_c(m, k) = \bar{P}_c, \\ & \quad P_c(m, k) \geq 0, \end{aligned} \quad (24)$$

with $m = 0, 1, \dots, M-1$ and $k = 0, 1, \dots, N_c-1$. For brevity, the ranges of values for m and k are omitted in sequel. Problem $\mathcal{P}1$ can be solved by using the Karush-Kuhn-Tucker (KKT) conditions, and the optimal solution is given by [41]

$$P_c(m, k) = \max \left\{ \frac{1}{\beta \ln 2} - \frac{\sigma_c^2}{|\hat{H}_c(m, k)|^2}, 0 \right\}, \quad (25)$$

where $\frac{1}{\beta \ln 2} = \frac{\bar{P}_c + \sum_{(m, k) \in \mathcal{N}_e} \frac{\sigma_c^2}{|\hat{H}_c(m, k)|^2}}{\text{card}(\mathcal{N}_e)}$ and \mathcal{N}_e contains the indices of all the REs with non-zero power, i.e., $P_c(m, k) > 0$.

Step 2. Sensing RE and power allocation: According to (25), if the (m, k) -th RE is under poor channel condition, i.e., $|\hat{H}_c(m, k)|^2$ is less than the threshold $\varsigma = \sigma_c^2 \beta \ln 2$, it will not be allocated for communication. By employing these inacti-

vated REs for sensing purpose, the time-frequency resources for both subsystems will be completely orthogonal without inducing mutual interference in principle, while ensuring the optimal communication performance. Accordingly, the matrix \mathbf{U} defined in (1) can be expressed as

$$U(m, k) = \begin{cases} 1, & \text{if } |\hat{H}_c(m, k)|^2 \leq \varsigma, \\ 0, & \text{if } |\hat{H}_c(m, k)|^2 > \varsigma. \end{cases} \quad (26)$$

Since the REs with good channel conditions are chosen for communication first, the sensing REs may be discontinuous in both time and frequency domains, causing possible high sidelobe in the ambiguity function. To reduce the sidelobe level for enhancing sensing performance, the power allocation strategy for sensing REs is to maximize the PSLR within Ω_s , which is formulated as

$$\mathcal{P}2: \begin{aligned} & \max_{\mathbf{P}_r} \frac{|\chi_a(0,0)|}{F(\Omega_s)}, \\ & \text{s.t. } \sum_{m=0}^{M-1} \sum_{k=0}^{N_c-1} P_r(m, k) = \bar{P}_r, \quad P_r(m, k) \geq 0, \end{aligned} \quad (27)$$

where \bar{P}_r is the total sensing power budget. Since the main peak $|\chi_a(0,0)|$ is always equal to the total sensing power $N_c \bar{P}_r$, the problem $\mathcal{P}2$ is equivalent to minimize the highest sidelobe level given by:

$$\mathcal{P}3: \begin{aligned} & \min_{\mathbf{P}_r} \max_{(0,0) \neq (\nu, \mu) \in \Omega_s} |\chi_a(\nu, \mu)|, \\ & \text{s.t. } \sum_{m=0}^{M-1} \sum_{k=0}^{N_c-1} P_r(m, k) = \bar{P}_r, \quad P_r(m, k) \geq 0. \end{aligned} \quad (28)$$

Due to the minimax form of the objective function, it is difficult to solve problem $\mathcal{P}3$ directly. To address this issue, a slack variable z_0 is introduced as the optimization objective. Accordingly, we add an extra constraint that all the sidelobes within Ω_s are less than z_0 . Then the optimization problem can be expressed as

$$\mathcal{P}4: \begin{aligned} & \min_{\mathbf{P}_r} z_0, \\ & \text{s.t. } |\chi_a(\nu, \mu)| < z_0, \quad (0, 0) \neq (\nu, \mu) \in \Omega_s, \\ & \quad \sum_{m=0}^{M-1} \sum_{k=0}^{N_c-1} P_r(m, k) = \bar{P}_r, \quad P_r(m, k) \geq 0. \end{aligned} \quad (29)$$

Problem $\mathcal{P}4$ now can be formulated into a quadratic problem, which is solvable using the CVX toolbox [42].

Step 3. PAPR reduction: In addition to the PSLR in the ambiguity function, the PAPR is also a significant metric for sensing sequences. A high PAPR results in nonlinear distortion of high power amplifier, which is detrimental especially for the millimeter wave and Terahertz bands [43]. To tackle this problem, we need to minimize the PAPR of the sensing sequence, whilst retaining the high PSLR property. Recall that the PSLR is mainly related to the power allocation \mathbf{P}_r according to (19), which inspires us to minimize the PAPR by optimizing the phase of each element of \mathbf{S}_r . Let $\theta(m, k)$ denote the phase of the symbol on the (m, k) -th RE. The PAPR of the sensing sequence corresponding to the m -th OFDM symbol

can be expressed as

$$\text{PAPR} = \frac{\max_{0 \leq n \leq N-1} \left| \sum_{k=0}^{N_c-1} U(m, k) \sqrt{P_r(m, k)} e^{j\theta(m, k) - 2\pi nk/N_c} \right|^2}{\sum_{k=0}^{N_c-1} U(m, k) P_r(m, k)}. \quad (30)$$

Because the PAPRs corresponding to different OFDM symbols are independent of each other, the phase-frequency characteristics of different OFDM symbols can be optimized separately. Consider the case that the phases of all the modulated symbols on different sensing REs are selected from the set $\{0, 2\pi/R, \dots, 2\pi(R-1)/R\}$ with the size R . Then the PAPR reduction problem for the m -th OFDM symbol can be formulated as

$$\mathcal{P}5: \begin{aligned} & \min_{\boldsymbol{\theta}_m} \max_n \left| \sum_{k=0}^{N_c-1} U(m, k) \sqrt{P_r(m, k)} e^{j\theta(m, k) - j2\pi nk/N_c} \right|^2, \\ & \text{s.t. } \theta(m, k) \in \{0, 2\pi/R, \dots, 2\pi(R-1)/R\}, \end{aligned} \quad (31)$$

where $\boldsymbol{\theta}_m = [\theta(m, 0), \theta(m, 1), \dots, \theta(m, N_c - 1)]^T$.

To solve this discrete optimization problem, we propose a heuristic searching method based on the BB algorithm to obtain a near optimal solution. The BB algorithm divides the whole feasible region into several sub-regions, which correspond to several sub-problems. For each sub-problem, well-designed functions are employed to estimate its upper and lower performance bounds. As the number of iterations increases, the minimum upper and lower bounds among all the sub-problems are obtained and updated. When the difference between the minimum upper and lower bounds is lower than a threshold, the iteration terminates and the solution that achieves the minimum upper bound is adopted as the final solution [44].

Let \mathbf{A}_m denote $e^{j\boldsymbol{\theta}_m}$, i.e., the k -th element of \mathbf{A}_m is $A_m(k) = e^{j\theta(m, k)}$. Since the feasible region of $A_m(k)$ is $\Phi = \{1, e^{j\frac{2\pi}{R}}, \dots, e^{j\frac{2\pi(R-1)}{R}}\}$, the whole feasible region of \mathbf{A}_m is $\Psi^{(0)} = \Phi^{N_c}$, which is the Cartesian product of N_c Φ s. The problem $\mathcal{P}5$ can be compactly written as

$$\mathcal{P}(\Psi^{(0)}): \begin{aligned} & \min_{\mathbf{A}_m} f(\mathbf{A}_m), \\ & \text{s.t. } \mathbf{A}_m \in \Psi^{(0)}, \end{aligned} \quad (32)$$

with

$$f(\mathbf{A}_m) = \max_n \left| \sum_{k=0}^{N_c-1} U(m, k) \sqrt{P_r(m, k)} A_m(k) e^{-j2\pi \frac{nk}{N_c}} \right|^2. \quad (33)$$

For each sub-region $\Psi \in \Psi^{(0)}$, denote its corresponding subproblem as $\mathcal{P}(\Psi)$. A lower bound of $\mathcal{P}(\Psi)$ can be derived by a bounding function, which can be expressed as

$$f_L(\Psi) = f(\mathbf{A}_m^L), \quad (34)$$

where \mathbf{A}_m^L is a relaxed solution of $\mathcal{P}(\Psi)$ that achieves the lower bound. More specifically, suppose that the first k_0 elements in Ψ remain in their original values, and its (k_0+1) -th element is fixed to a feasible value. By extending the feasible region of the other elements to a continuous search region, a

Algorithm 1 PAPR reduction method based on BB algorithm

Input: Sensing power allocation \mathbf{P}_r , indicating matrix \mathbf{U} , termination threshold ϵ , pruning threshold N_s ;

- 1: Initialization: $\mathcal{S} = \{\mathcal{P}(\Psi^{(0)})\}$, $B_L = f_L(\Psi^{(0)})$, $B_U = f_U(\Psi^{(0)})$;
- 2: **while** $B_U - B_L > \epsilon$ and $\mathcal{S} \neq \emptyset$ **do**
- 3: **Branching:** Select $\mathcal{P}(\Psi) \in \mathcal{S}$ such that $f_L(\Psi)$ is the smallest;
- 4: **if** Ψ is non-divisible **then**
- 5: Delete $\mathcal{P}(\Psi)$ from \mathcal{S} ;
- 6: Continue; (go to line 3 **Branching**)
- 7: **end if**
- 8: Partition Ψ into R sub-regions $\Psi_1, \Psi_2, \dots, \Psi_R$ according to (38);
- 9: Delete $\mathcal{P}(\Psi)$ from \mathcal{S} ;
- 10: Add $\mathcal{P}(\Psi_1), \mathcal{P}(\Psi_2), \dots, \mathcal{P}(\Psi_R)$ to \mathcal{S} ;
- 11: **Bounding:** According to (34) and (37), calculate the lower and upper bounds for $\mathcal{P}(\Psi_r)$, $r = 1, 2, \dots, R$;
- 12: Update B_U and B_L ;
- 13: **Pruning:** If the lower bound of $\mathcal{P}(\Psi_r)$ is larger than B_U , delete $\mathcal{P}(\Psi_r)$ from \mathcal{S} ;
- 14: **while** $\text{card}(\mathcal{S}) > N_s$ **do**
- 15: Delete the sub-problem with the largest lower bound from \mathcal{S} ;
- 16: **end while**
- 17: **end while**
- 18: **return** $\boldsymbol{\theta}_m = \text{angle}(\mathbf{A}_m^{\text{opt}})$ with $f(\mathbf{A}_m^{\text{opt}}) = B_U$.

relaxed problem $\mathcal{P}_L(\Psi)$ can be expressed as

$$\begin{aligned} \mathcal{P}_L(\Psi) : \min_{A_m(k_0+1), \dots, A_m(N_c-1)} & f(\mathbf{A}_m), \\ \text{s.t.} & |A_m(k)|^2 \leq 1, \end{aligned} \quad (35)$$

with $k = k_0 + 1, k_0 + 2, \dots, N_c - 1$. \mathbf{A}_m^L can be derived by solving $\mathcal{P}_L(\Psi)$ via the CVX toolbox, yielding the lower bound $f_L(\Psi)$ of each sub-problem. On the other hand, by projecting \mathbf{A}_m^L onto its closest feasible point, i.e.,

$$\mathbf{A}_m^U = \arg \min_{\mathbf{A}_m \in \Psi^{(0)}} \|\mathbf{A}_m - \mathbf{A}_m^L\|, \quad (36)$$

an upper bound of each sub-problem is obtained, which can be written as

$$f_U(\Psi) = f(\mathbf{A}_m^U). \quad (37)$$

The proposed PAPR reduction procedure is summarized in Algorithm 1. We initialize the problem set \mathcal{S} as $\{\mathcal{P}(\Psi^{(0)})\}$. The minimum upper bound B_U and lower bound B_L are initialized as the upper and lower bounds of $\mathcal{P}(\Psi^{(0)})$, respectively. At each iteration, the sub-problem $\mathcal{P}(\Psi)$ with the smallest lower bound in \mathcal{S} is selected. Note that the first k_0 elements of \mathbf{A}_m in Ψ have been set to fixed values in the previous iterations. If $k_0 = N_c$, i.e., all the elements of \mathbf{A}_m have already been set to fixed values, Ψ is non-divisible and $\mathcal{P}(\Psi)$ is deleted from \mathcal{S} , and the algorithm considers the next smallest lower-bound subproblem in \mathcal{S} . Otherwise, by denoting the fixed value of $A_m(k)$ as $a_k \in \Phi$, the region Ψ can be expressed as

$\Psi = \{a_0\} \otimes \{a_1\} \otimes \dots \otimes \{a_{k_0-1}\} \otimes \Phi^{N_c-k_0} \triangleq \Psi^{[k_0]} \otimes \Phi^{N_c-k_0}$, where \otimes denotes the Cartesian product. Ψ is divided into R smaller regions by fixing the $(k_0 + 1)$ -th element of \mathbf{A}_m to each of the R values in ϕ , while the feasible region of the remaining elements of \mathbf{A}_m is the full search region Φ , which can be expressed as

$$\begin{aligned} \Psi_1 &= \Psi^{[k_0]} \otimes \{1\} \otimes \Phi^{N_c-k_0-1}, \\ \Psi_2 &= \Psi^{[k_0]} \otimes \{e^{j\frac{2\pi}{R}}\} \otimes \Phi^{N_c-k_0-1}, \\ &\dots, \\ \Psi_R &= \Psi^{[k_0]} \otimes \{e^{j\frac{2\pi(R-1)}{R}}\} \otimes \Phi^{N_c-k_0-1}. \end{aligned} \quad (38)$$

Their corresponding problems, $\mathcal{P}(\Psi_1), \mathcal{P}(\Psi_2), \dots, \mathcal{P}(\Psi_R)$, are added to \mathcal{S} and the problem $\mathcal{P}(\Psi)$ is deleted from \mathcal{S} . The lower and upper bounds of each of these created sub-problems are calculated by bounding functions to update B_L and B_U . If the lower bound of a certain sub-problem is larger than B_U , it is deleted from \mathcal{S} . To reduce the worst-case computational complexity, we also keep $\text{card}(\mathcal{S})$ to no more than a threshold N_s by deleting sub-problems with relatively larger lower bound from \mathcal{S} . When the difference between B_L and B_U is less than a threshold ϵ or \mathcal{S} is an empty set, the iteration procedure terminates. The solution corresponding to B_U is the final solution $\mathbf{A}_m^{\text{opt}}$, and the symbol phase $\boldsymbol{\theta}_m$ is set as $\text{angle}(\mathbf{A}_m^{\text{opt}})$. As it can be seen, the worst-case computational complexity of the proposed PAPR reduction is $\mathcal{O}(\text{card}(\mathcal{S})N_c)$, which is much lower than the computation complexity of exhaustive searching ($\mathcal{O}(R^{N_c})$). Besides, based on the design requirement, the computational complexity can be further reduced by adjusting the parameter ϵ .

IV. SENSING-CENTRIC ISAC WAVEFORM DESIGN

In this design, we first adjust the unit cells of the ambiguity function within its RoI to guarantee the ‘locally’ perfect auto-correlation property that ensures the sensing sequence having no sidelobes within the RoI. Based on the correspondence between the main part of the ambiguity function and the sensing power allocation strategy, the irrelevant cells beyond RoI determine the sensing power allocation strategy. Then REs with relatively low power budget are assigned for communications. Then the irrelevant cells are optimized together with the communication power allocation strategy for throughput enhancement in an alternating iterative manner.

A. Problem Formulation

To provide accurate sensing, the sidelobe level in the ambiguity function can be adopted to characterize sensing performance, as mentioned in Section III. A sensing sequence has a locally perfect auto-correlation property, when the value of the highest sidelobe within RoI in its ambiguity function is zero, which can be expressed as

$$|\chi_a(\nu, \mu)| = \gamma(\nu, \mu)\eta(\nu) = 0, \quad (0, 0) \neq (\nu, \mu) \in \Omega_s. \quad (39)$$

Since $\eta(\nu) \neq 0$ (when $m > 1$), $|\chi_a(\tau, \nu)| = 0$ is equivalent to $\gamma(\nu, \mu) = 0$. Given the total sensing power

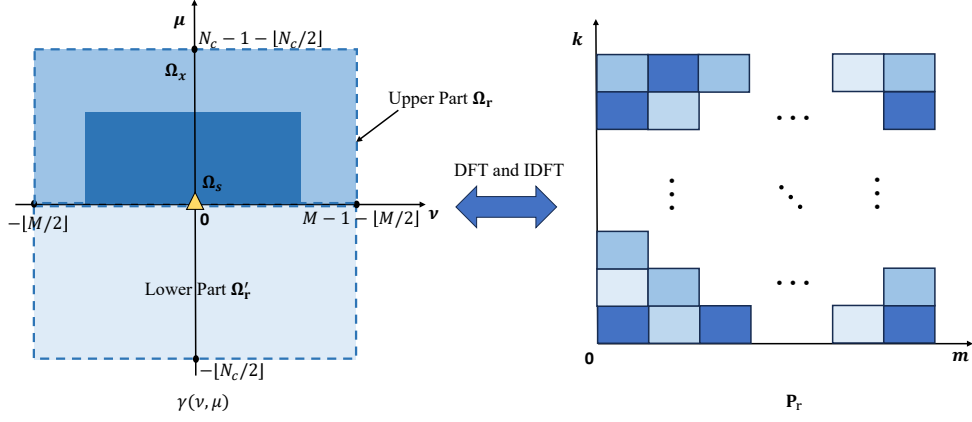


Fig. 3. One to one mapping between $\gamma(v, \mu)$ and \mathbf{P}_r . The left figure illustrates different regions of $\gamma(v, \mu)$, and the right figure shows the sensing power allocation \mathbf{P}_r , where the depth of the color indicates the amount of power for the (m, k) -th RE.

$\sum_{m=0}^{M-1} \sum_{k=0}^{N_c-1} P_r(m, k) = \bar{P}_r$, $\gamma(0, 0)$ is always equal to \bar{P}_r . Therefore, the locally perfect auto-correlation property can be obtained by setting the function $\gamma(v, \mu)$ within RoI as

$$\gamma(v, \mu) = \begin{cases} \bar{P}_r, & (v, \mu) = (0, 0), \\ 0, & (0, 0) \neq (v, \mu) \in \Omega_s. \end{cases} \quad (40)$$

According to (20), $\gamma(v, \mu)$ is derived by performing DFT and IDFT on $P_r(m, k)$ along its column and row, respectively. Therefore, $P_r(m, k)$ can be derived by performing inverse operations on $\gamma(v, \mu)$, which can be expressed as

$$P_r(m, k) = \frac{1}{MN_c} \sum_{\nu=-[M/2]}^{M-1-[M/2]} \sum_{\mu=-[N_c/2]}^{N_c-1-[N_c/2]} \gamma(v, \mu) e^{j2\pi \frac{\mu k}{N_c}} e^{-j2\pi \frac{\nu m}{M}}. \quad (41)$$

Since there is a one-to-one mapping between $\gamma(v, \mu)$ and $P_r(m, k)$, we can use $\gamma(v, \mu)$ as the optimization variable instead of $P_r(m, k)$ to reduce the dimension of the optimization variable. This is because for a sensing with a locally perfect auto-correlation property, the unit cells of $\gamma(v, \mu)$ within Ω_s are fixed and we only need to optimize the unit cells in the complementary set of Ω_s , which are called irrelevant cells. $P_r(m, k)$ is always a non-negative real number, the irrelevant cells should be designed under this constraint, which is formulated as

$$\begin{aligned} \mathcal{P}8: \quad & \text{find } \gamma(v, \mu), \text{ for } (v, \mu) \in \bar{\Omega}_s, \\ & \text{s.t. } P_r(m, k) \geq 0, \\ & \quad P_r(m, k) = P_r^*(m, k), \end{aligned} \quad (42)$$

where $\bar{\Omega}_s$ denotes the complementary set of Ω_s in Ω , and $P_r(m, k) = P_r^*(m, k)$ is equivalent to $\gamma(v, \mu)$ being centro-hermitian symmetric, which can be expressed as

$$\gamma(v, \mu) = \gamma^*(-\nu, -\mu), \quad (v, \mu) \in \Omega. \quad (43)$$

As seen in Fig. 3, the upper part Ω_r and lower part Ω_r' of the ambiguity function divided by the v -axis are mutually centro symmetric. Therefore, we only need to adjust the upper part denoted by $\Omega_r = [-[M/2], -[M/2] + 1, \dots, M - 1 - [M/2]] \times [0, 1, \dots, N_c - 1 - [N_c/2]]$. Ω_r consists of the RoI

Ω_s and the outer region Ω_x . Since the unit cells in Ω_s are fixed to ensure perfect auto-correlation property locally, the unit cells in Ω_x are finally employed as the optimization variables, which can be expressed as

$$\begin{aligned} \mathcal{P}9: \quad & \text{find } \gamma(v, \mu), \text{ for } (v, \mu) \in \Omega_x, \\ & \text{s.t. } P_r(m, k) \geq 0. \end{aligned} \quad (44)$$

Specifically, Ω_x can be expressed as Ω_r / Ω_s , where $/$ denotes the difference operation between sets. For brevity, $(v, \mu) \in \Omega_x$ is omitted below, i.e., the optimization of $\gamma(v, \mu)$ is referred to as the optimization of the unit cells of $\gamma(v, \mu)$ in Ω_x . Each solution to the problem $\mathcal{P}9$ corresponds to one of the possible realizations of \mathbf{P}_r , which can all realize locally perfect auto-correlation property to guarantee superior sensing performance. The REs with relatively low sensing power budget, i.e., lower than a predefined threshold δ , are considered to have a marginal impact on the sensing task. Hence, these REs are assigned for data transmission, where the indicating matrix \mathbf{U} can be written as

$$U(m, k) = \begin{cases} 1, & \text{if } P_r(m, k) > \delta, \\ 0, & \text{if } P_r(m, k) \leq \delta. \end{cases} \quad (45)$$

Afterward, the power allocation for different communication REs is optimized for achievable data rate maximization. In this way, the achievable data rate is related to both the irrelevant cells of $\gamma(v, \mu)$ and the communication power strategy. The jointly optimization can be derived by combining problem $\mathcal{P}9$ and communication power allocation, which can be expressed as

$$\begin{aligned} \mathcal{P}11: \quad & \max_{\gamma(v, \mu), \mathbf{P}_c} \sum_{m=0}^{M-1} \sum_{k=0}^{N_c-1} \log \left(1 + \frac{(1-U(m, k))P_c(m, k)|\hat{H}_c(m, k)|^2}{\sigma_c^2} \right), \\ & \text{s.t. } \sum_{m=0}^{M-1} \sum_{k=0}^{N_c-1} P_c(m, k) = \bar{P}_c, \quad P_c(m, k) \geq 0, \\ & \quad P_r(m, k) \geq 0. \end{aligned} \quad (46)$$

One intuitive method of solving problem $\mathcal{P}11$ is to exhaustively search for the values of $\gamma(v, \mu)$ within Ω_x , which however imposes considerable computational complexity. On the other hand, since there are two types of optimization variables and

the last constraint of the problem is non-convex, it is difficult to solve the problem via the KKT conditions directly. We propose a low-complexity alternating optimization algorithm to solve problem \mathcal{P}_{11} with near optimal solution.

B. Alternating Optimization Algorithm

\mathcal{P}_{11} can be naturally divided into two sub-problems, the communication power allocation problem and the irrelevant cell design problem, which corresponds to the optimization of \mathbf{P}_c and the irrelevant cells of $\gamma(\nu, \mu)$, respectively. For tractability of solving \mathcal{P}_{11} , we optimize these two variables alternatively in an iterative manner. Denote the variables optimized after the i -th iteration as $\mathbf{P}_c^{(i)}$ and $\gamma^{(i)}(\nu, \mu)$. Accordingly, $\mathbf{P}_r^{(i)}$ and $\mathbf{U}^{(i)}$ can be calculated based on $\gamma^{(i)}(\nu, \mu)$ according to (41) and (45). Further denote the maximum achievable data rate in the i -th iteration as $r^{(i)}$. At the beginning, we initialize $\gamma(\nu, \mu)$ as $\gamma^{(0)}(\nu, \mu)$. How to do this is discussed in (52) at the end of this subsection. In the i -th iteration, the optimization of \mathbf{P}_c is formulated as

$$\begin{aligned} \mathcal{P}_{12} : \max_{\mathbf{P}_c} \sum_{m=0}^{M-1} \sum_{k=0}^{N_c-1} \log \left(1 + \frac{(1-U^{(i-1)}(m, k))P_c(m, k)|\hat{H}_c(m, k)|^2}{\sigma_c^2} \right), \\ \text{s.t. } \sum_{m=0}^{M-1} \sum_{k=0}^{N_c-1} P_c(m, k) = \bar{P}_c, \quad P_c(m, k) \geq 0. \end{aligned} \quad (47)$$

On the other hand, the optimization of the irrelevant cells of $\gamma(\nu, \mu)$ can be expressed as

$$\begin{aligned} \mathcal{P}_{13} : \max_{\gamma(\nu, \mu)} \sum_{m=0}^{M-1} \sum_{k=0}^{N_c-1} \log \left(1 + \frac{(1-U(m, k))P_c^{(i)}(m, k)|\hat{H}_c(m, k)|^2}{\sigma_c^2} \right), \\ \text{s.t. } P_r(m, k) \geq 0. \end{aligned} \quad (48)$$

The sub-problem \mathcal{P}_{12} can be solved by employing the KKT conditions, and the optimal solution is given by

$$P_c^{(i)}(m, k) = \begin{cases} \max \left\{ \frac{1}{\beta \ln 2} - \frac{\sigma_c^2}{|\hat{H}_c(m, k)|^2}, 0 \right\}, & U^{(i-1)}(m, k) = 0, \\ 0, & U^{(i-1)}(m, k) = 1, \end{cases} \quad (49)$$

where $\frac{1}{\beta \ln 2} = \frac{\bar{P}_c + \sum_{(m, k) \in \mathcal{N}_e} \frac{\sigma_c^2}{|\hat{H}_c(m, k)|^2}}{\text{card}(\mathcal{N}_e)}$ and \mathcal{N}_e contains the indices of all the REs with non-zero power, i.e., $P_c^{(i)}(m, k) > 0$ [41]. By contrast, the solution of the sub-problem \mathcal{P}_{13} is challenging to obtain, because the mapping function between $U(m, k)$ and $P_r(m, k)$ is discontinuous and non-convex. To tackle this issue, an intuitive approach is to employ a linear continuous function of $P_r(m, k)$ to approximate $U(m, k)$, which can be expressed as $U(m, k) \approx P_r(m, k)/A$, where A is a normalization factor of $P_r(m, k)$ and can be set as the largest element of $\mathbf{P}_r^{(0)}$. Obviously, this is a rough approximation. But by carefully selecting the range of values for $P_r(m, k)$, it can be made a tight approximation. More specifically, if the value of $P_r(m, k)$ is close to 0 or A , the error of the linear approximation is negligible. Considering $0 \leq P_r(m, k) \leq A$, the term $P_r(m, k)(1 - P_r(m, k)/A)$ can be used to indicate how close $P_r(m, k)$ is to 0 or A . If $P_r(m, k)$ is equal to 0 or A , the term is equivalent to 0. On the other hand, if $P_r(m, k)$

is significantly different from both 0 and A , the value of the term becomes large. Therefore, $-P_r(m, k)(1 - P_r(m, k)/A)$ is added to the optimization objective of \mathcal{P}_{13} as a penalty term, which then becomes:

$$\begin{aligned} \mathcal{P}_{14} : \max_{\gamma(\nu, \mu)} \sum_{m=0}^{M-1} \sum_{k=0}^{N_c-1} \log \left(1 + \frac{(1 - \frac{P_r(m, k)}{A})P_c^{(i)}(m, k)|\hat{H}_c(m, k)|^2}{\sigma_c^2} \right) \\ - \lambda P_r(m, k) \left(1 - \frac{P_r(m, k)}{A} \right), \\ \text{s.t. } 0 \leq P_r(m, k) \leq A, \end{aligned} \quad (50)$$

where λ is a weight factor that trades off between the achievable data rate and the requirement for the range of values for $P_r(m, k)$.

Since the optimization objective of \mathcal{P}_{14} is not a concave function, \mathcal{P}_{14} is difficult to maximize directly. To tackle this issue, a lower bound of the optimization objective is derived by converting the second term $P_r(m, k)(1 - P_r(m, k)/A)$ with its linear approximation. According to the Minorize-Maximization (MM) algorithm, by maximizing the lower bound in each iteration, the results will finally converge to the optimal solution of the original problem [45]. Therefore, we maximize the lower bound of the optimization objective iteratively, where the problem in the j -th iteration can be formulated as

$$\begin{aligned} \mathcal{P}_{15} : \max_{\gamma(\nu, \mu)} \sum_{m=0}^{M-1} \sum_{k=0}^{N_c-1} \log \left(1 + \frac{(1 - \frac{P_r(m, k)}{A})P_c^{(i)}(m, k)|\hat{H}_c(m, k)|^2}{\sigma_c^2} \right) \\ - \lambda \left(P_r(m, k) - \frac{2P_r^{(i, j-1)}(m, k)}{A} P_r(m, k) \right), \\ \text{s.t. } 0 \leq P_r(m, k) \leq A. \end{aligned} \quad (51)$$

$P_r^{(i, j-1)}(m, k)$ is calculated based on the optimization results $\gamma^{(i, j-1)}(\nu, \mu)$ in the $(j-1)$ -th iteration. Besides, we denote the optimization result of the objective function in the $(j-1)$ -th iteration as $\bar{r}^{(i, j-1)}$. If j is larger than the maximum number of iteration J_m , or $|\bar{r}^{(i, j)} - \bar{r}^{(i, j-1)}|$ is less than a predefined threshold ϵ_2 , the iteration procedure is terminated, and the value of $\gamma^{(i)}(\nu, \mu)$ is obtained as $\gamma^{(i, j)}(\nu, \mu)$. Given the non-convex nature of problem \mathcal{P}_{11} , the convergence of the alternating iterative algorithm depends on the initial value. To strike a balance between computational complexity and the optimality of the solution, it is advisable to select an initial value that is not only easy to obtain but also reasonably close to the optimal solution. Following this philosophy, we derive the initial value $\gamma^{(0)}(\nu, \mu)$ by solving the following problem:

$$\begin{aligned} \mathcal{P}_{16} : \min_{\gamma(\nu, \mu)} \sum_{m=0}^{M-1} \sum_{k=0}^{N_c-1} P_r(m, k)|\hat{H}_c(m, k)|^2, \\ \text{s.t. } P_r(m, k) \geq 0, \end{aligned} \quad (52)$$

which is a linear programming problem, and can be readily solved with low complexity. The objective function aims to allocate low sensing power to REs with high communication channel gains, i.e., $|\hat{H}_c(m, k)|^2$ is large. This avoids the sensing subsystem to occupy high-quality communication channels, while ensuring the optimal sensing performance.

The complete procedure of sensing-centric ISAC waveform design is given in Algorithm 2. The main computation complexity of Algorithm 2 lies in the two iterations corresponding

Algorithm 2 Sensing-centric waveform design procedure

Input: Total communication power \bar{P}_c , total sensing power \bar{P}_r , estimated communication channel \hat{H}_c , region of interest Ω_s , maximum number of alternating iterations I_m , maximum number of inner iterations J_m , termination thresholds for outer and inner loops ϵ_1 and ϵ_2 ;

- 1: Initialize $\gamma^{(0)}(\nu, \mu)$, $\mathbf{P}_r^{(0)}$ and $\mathbf{U}^{(0)}$ according to $\mathcal{P}16$, (41) and (45);
- 2: **while** $i \leq I_m$ or $|r^{(i)} - r^{(i-1)}| < \epsilon_1$ **do**
- 3: Allocate the communication power $\mathbf{P}_c^{(i)}$ according to $\mathcal{P}12$;
- 4: **while** $j \leq J_m$ or $|\bar{r}^{(i,j)} - \bar{r}^{(i,j-1)}| < \epsilon_2$ **do**
- 5: Calculate $\gamma^{(i,j)}(\mathbf{P}_r, \nu, \mu)$, $\mathbf{P}_r^{(i,j)}$ according to $\mathcal{P}14$;
- 6: $j = j + 1$;
- 7: **end while**
- 8: Calculate $\mathbf{U}^{(i)}$ according to (45);
- 9: $i = i + 1$;
- 10: **end while**
- 11: **return** \mathbf{P}_c , \mathbf{P}_r , \mathbf{U} .

to Line 2 and Line 4, and the total iteration number is no more than $I_m J_m$. In our simulation, when $\epsilon_1 = 10^{-3}$ and $\epsilon_2 = 10^{-1}$, the total iteration number is less than 20 with the probability of 90%.

V. NUMERICAL RESULTS

Numerical results are provided to validate the proposed communication-centric and sensing-centric waveform designs and to provide useful guidelines for the implementation of the proposed designs. The simulation system parameters are listed in Table I.

A. Communication-centric Design

Fig. 4 presents the ambiguity function of the sensing component generated by our proposed communication-centric waveform design. The sensing scopes of distance and speed are set as $[0, 60]$ m and $[-20, 20]$ m/s, respectively. The corresponding

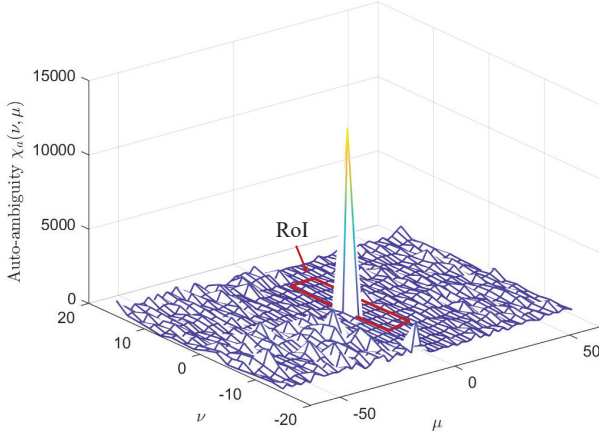


Fig. 4. Ambiguity function of the proposed communication-centric waveform.

TABLE I
SYSTEM PARAMETERS

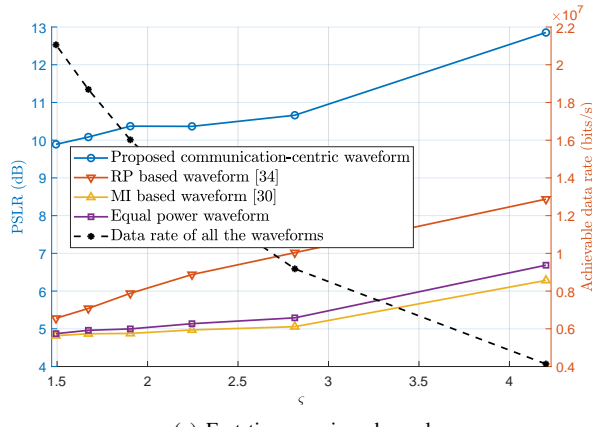
Symbol	Parameter	Value
f_c	Carrier frequency	240 GHz
Δf	Subcarrier spacing	240 kHz
N_c	Number of subcarrier	128
T	OFDM symbol duration	$4.1470 \mu\text{s}$
T_G	Cyclic prefix length	$1.0368 \mu\text{s}$
T_O	Total OFDM symbol duration	$5.1838 \mu\text{s}$
M	Number of OFDM symbol	32
d_m	Maximum range	155 m
v_m	Maximum relative speed	$\pm 60 \text{ m/s}$

RoI is derived according to (22), which is outlined with red lines in Fig. 4. It can be seen that since there are non-negligible sidelobes outside the RoI, the PSLR in the whole ambiguity function is 7 dB. However, the level of sidelobes within the RoI is marginal, leading to a PSLR of 12 dB within the RoI. Therefore, the proposed communication-centric waveform can guarantee superior sensing performance within the RoI, whilst attaining the maximum data throughput at the same time.

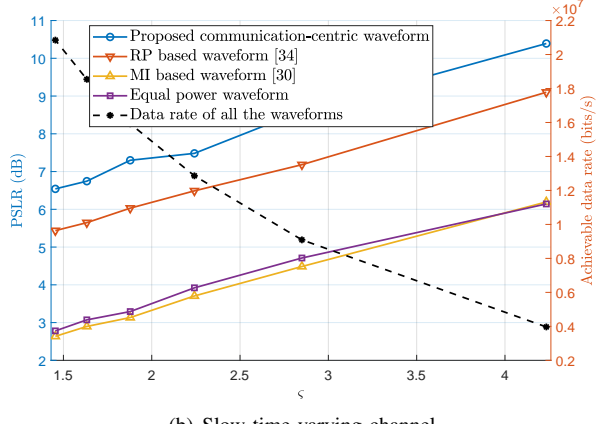
Fig. 5 illustrates the sensing and communication performance of the proposed communication-centric waveform and three existing designs, in terms of the PSLR within the RoI and the achievable data rate, where a wide range of the channel quality threshold ς is adopted. The fast and slow time-varying channels are considered in Figs. 5(a) and 5(b), respectively, with the former having a larger Doppler frequency offset range (~ 100 kHz) than the latter (~ 1 kHz). The three existing designs compared are the range profile (RP) based waveform [34], the MI based waveform [30], and the equal power waveform. Specifically, the RP based waveform allocates the sensing power to each OFDM symbol separately and optimizes the PSLR in the range profile, the MI based waveform optimizes the MI between the target impulse response and the received signal, while the equal power waveform evenly distributes the sensing power among the sensing REs.

For a fair comparison, all the four waveforms are based on the communication-centric criterion. In other words, for a given communication power \bar{P}_c , all the four ISAC waveforms are designed by firstly allocating REs with high-quality channel conditions, i.e., $\|\hat{H}_c(m, k)\|^2 \geq \varsigma$, for data transmission. Therefore, the achievable data rates of all the four ISAC waveforms are the same, which is referred to as ‘data rate of all the waveforms’ and corresponds to the black dashed curve in Figs. 5(a) and 5(b). It is observed that as the threshold ς increases, fewer REs are allocated to communications, and this results in a decrease in the achievable data rate.

By contrast, as ς increases, more REs are allocated to sensing, and this leads to an increase in the PSLR within the RoI. It can be seen that the proposed communication-centric waveform is capable of significantly improving the PSLR compared with the three benchmark waveforms in both fast and slow fading channels. In the slow fading channel, where the channel condition for each OFDM symbol remains nearly unchanged



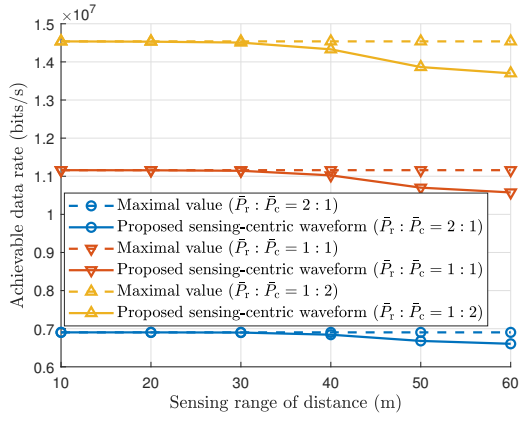
(a) Fast time-varying channel



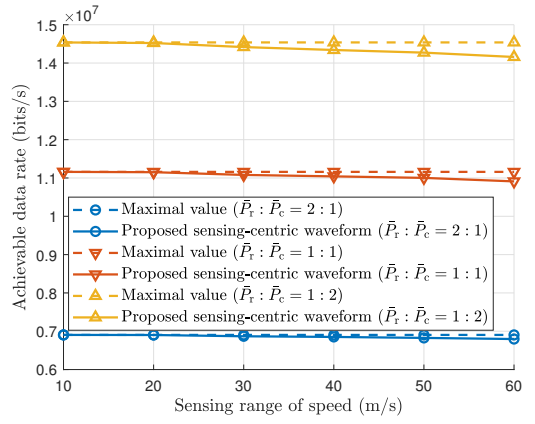
(b) Slow time-varying channel

Fig. 5. Sensing and communication performance of the proposed communication-centric waveform and existing designs as the function of the channel quality threshold ζ .

within a frame, our proposed waveform improves the PSLR by about 1 dB compared to the RP based waveform. Conversely, in the fast fading channel, where the channel conditions among OFDM symbols vary quickly, the joint design over multiple OFDM symbols is necessary for sensing performance enhancement. In this case, our proposed waveform improves the PSLR by nearly 5 dB over the second best RP based waveform. By comparing Fig. 5(a) with Fig. 5(b), it can be seen that the PSLR performance of the three existing designs in the fast fading channel situation are generally worst than their PSLR performance in the slow fading channel scenario, which is to be expected. However, the PSLR performance of our proposed design is actually better in the fast fading case than in the slow fading one. The reason for this ‘unexpected’ phenomenon can be explained as follows. In the slow fading channel, due to the relatively stable channel conditions, certain subcarriers under high-quality channel may remain allocated for communications within multiple consecutive OFDM symbols. Accordingly, the sensing subsystem is unable to employ these subcarriers throughout the whole processing interval, which induces high sidelobes in the ambiguity function. By contrast, in the fast fading channel, the RE allocation between communication and sensing subsystems changes dynamically



(a) Achievable data rate with sensing range of distance



(b) Achievable data rate with sensing range of speed

Fig. 6. Achievable data rate with respect to the sensing range of distance and speed, in comparison with the maximal data rate. The sensing range of speed is set as $[-60, 60]$ m/s in (a) and the sensing range of distance is set as $[0, 60]$ m in (b).

across multiple OFDM symbols, allowing the sensing subsystem to utilize diverse subcarriers at different instants in the processing interval. Then through our proposed joint multi-symbol power optimization, the sensing system is capable of effectively integrating information from different subcarriers, resulting in an increase in the PSLR within the RoI, compared with the slow fading case. Furthermore, through the proposed PAPR reduction method of Algorithm 1, our communication-centric waveform manages to obtain acceptable PAPR levels of 5.83 dB (when employing binary PSK) and 4.81 dB (when employing quadrature PSK), which achieves more than 8 dB PAPR reduction over those without phase adjustment.

B. Sensing-centric Design

Figs. 6(a) and 6(b) compare the achievable data rates of the proposed sensing-centric waveform with that of the baseline with respect to the sensing ranges of distance and speed, respectively, where different ratios of the sensing power to the communication power are considered. More specifically, the baseline, referred to as ‘maximal value’, is set to an upper bound of the achievable data rate obtained by maximizing

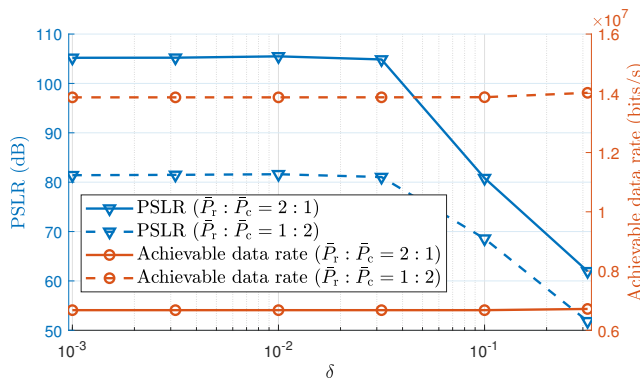


Fig. 7. PSLR and achievable data rate with respect to δ , where $\lambda = 0.02$ and the sensing ranges of distance and speed are set as $[0, 50]$ m and $[-60, 60]$ m/s, respectively.

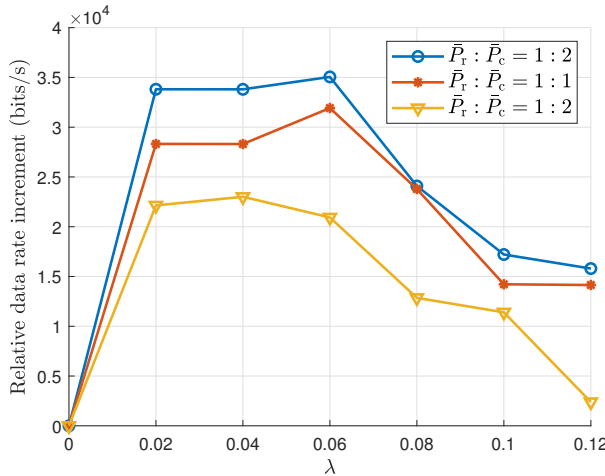


Fig. 8. Relative data rate increment with respect to λ , where $\delta = 0.03$ and the sensing ranges of distance and speed are set as $[0, 50]$ m and $[-60, 60]$ m/s, respectively.

the communication performance without the consideration of sensing. As expected, both the achievable data rates of our proposed waveform and the baseline increase with the decrease in the ratio of the sensing power to the communication power, since more power is allocated to the communication subsystem. On the other hand, as the sensing ranges of distance and speed increase, i.e., the RoI becomes larger, the number of irrelevant cells decreases, which results in the reduction of the dimension of optimization variables for communication performance. Therefore, the achievable data rate of our proposed waveform degrades slightly with the increase in sensing ranges of distance and speed. However, the achieved data rate of our sensing-centric waveform still closely approaches the maximal value when the sensing ranges of distance and speed are no more than 40 m and ± 50 m/s, respectively, which validates the feasibility and effectiveness of Algorithm 2.

Fig. 7 investigates the sensing and communication performances of the proposed sensing-centric waveform, in terms of the PSLR within the RoI and the achievable data rate,

with respect to the sensing power threshold δ for each RE. Specifically, the PSLRs within the RoI under different ratios of the sensing power to the communication power are illustrated by the blue curves, while the achievable data rates are illustrated by the orange curves. It can be seen that the PSLR degrades with the increase of δ when δ is larger than 0.03. This is because more REs are designated for the communication subsystem, even though some of them have significant impact on the sensing performance. On the other hand, when δ is between 10^{-3} to 10^{-1} , the achievable data rate exhibits only a very marginal improvement as δ increases. This is attributed to the fact that the additional communication REs may operate under unfavorable channel conditions. Consequently, we can set δ between 10^{-3} and 0.03 in order to achieve a good trade-off in the RE assignment that guarantees the optimal sensing performance and high-rate communication simultaneously.

Fig. 8 presents the communication performance of our proposed sensing-centric waveform, in terms of the relative data rate increment with respect to λ , which is the weighting factor of the penalty term in \mathcal{P}_{14} . The relative data rate increment is calculated as the difference between the current achievable data rate and the data rate at $\lambda = 0$. As λ increases, we observe a significant rise in the achievable data rate when λ is less than 0.02, followed by a rapid decline when $\lambda > 0.06$. This is because when $\lambda < 0.02$, the penalty term cannot effectively constrain the values of $P_r(m, k)$, reducing λ leads to a larger approximation error that negatively impacts the achievable data rate. On the other hand, when $\lambda > 0.06$, the penalty term outweighs the data rate maximization, and increasing λ degrades the communication performance. Therefore, in this example, λ can be set between 0.02 and 0.06 numerically to balance the penalty term and communication performance.

VI. CONCLUSION

In this paper, a cross-domain OFDM-IS-based ISAC waveform design methodology, including communication- and sensing-centric waveform designs, was proposed for sensing and communication performance enhancement. In the communication-centric waveform design, a fraction of REs were assigned for communications for the maximization of the achievable data rate and the remaining REs were employed by the sensing subsystem with optimized power- and phase-domain coefficients. For the sensing-centric design, the ambiguity function value within the RoI of the integrated waveform was designed to have a ‘locally’ perfect auto-correlation property. Afterwards, the ambiguity function values in the irrelevant cells and the communication power allocation were jointly optimized for the achievable data rate enhancement through an alternating optimization algorithm. Numerical results showed that the proposed communication-centric waveform achieves significantly higher PSLR with the optimal achievable data rate and low PAPR, compared with the existing ISAC waveform designs. Moreover, the proposed sensing-centric waveform approaches the maximum achievable data rate while providing a ‘locally’ perfect auto-correlation property by carefully choosing the key parameters.

REFERENCES

- [1] F. Zhang, T. Mao, R. Liu, Z. Han, O. A. Dobre, S. Chen, and Z. Wang, "Cross-domain multicarrier waveform design for integrated sensing and communication," [Online] Available: <https://www.researchgate.net/publication/374950217>, 2023.
- [2] L. Bariah, *et al.*, "A prospective look: Key enabling technologies, applications and open research topics in 6G networks," *IEEE Access*, vol. 8, pp. 174792–174820, 2020.
- [3] W. Saad, M. Bennis, and M. Chen, "A vision of 6G wireless systems: Applications, trends, technologies, and open research problems," *IEEE Netw.*, vol. 34, no. 3, pp. 134–142, May 2020.
- [4] M. Z. Chowdhury, M. Shahjalal, S. Ahmed, and Y. M. Jang, "6G wireless communication systems: Applications, requirements, technologies, challenges, and research directions," *IEEE Open J. Commun. Soc.*, vol. 1, pp. 957–975, Jul. 2020.
- [5] R. Liu, R. Y.-N. Li, M. D. Renzo, and L. Hanzo, "A vision and an evolutionary framework for 6G: Scenarios, capabilities and enablers," *arXiv e-prints*, arXiv:2305.13887, May 2023.
- [6] C. Sturm and W. Wiesbeck, "Waveform design and signal processing aspects for fusion of wireless communications and radar sensing," *Proc. IEEE*, vol. 99, no. 7, pp. 1236–1259, Jul. 2011.
- [7] H. Zhang, *et al.*, "Holographic integrated sensing and communication," *IEEE J. Sel. Areas Commun.*, vol. 40, no. 7, pp. 2114–2130, Jul. 2022.
- [8] X. Yu, Q. Yang, Z. Xiao, H. Chen, V. Havyarimana, and Z. Han, "A precoding approach for dual-functional radar-communication system with one-bit DACs," *IEEE J. Sel. Areas Commun.*, vol. 40, no. 6, pp. 1965–1977, Jun. 2022.
- [9] F. Liu, *et al.*, "Joint radar and communication design: Applications, state-of-the-art, and the road ahead," *IEEE Trans. Commun.*, vol. 68, no. 6, pp. 3834–3862, Jun. 2020.
- [10] Y. Liu, I. Al-Nahhal, O. A. Dobre, and F. Wang, "Deep-learning channel estimation for IRS-assisted integrated sensing and communication System," *IEEE Trans. Veh. Technol.*, vol. 72, no. 5, pp. 6181–6193, May 2023.
- [11] Y. Cui, F. Liu, X. Jing, and J. Mu, "Integrating sensing and communications for ubiquitous IoT: Applications, trends, and challenges," *IEEE Netw.*, vol. 35, no. 5, pp. 158–167, Nov. 2021.
- [12] F. Liu, *et al.*, "Integrated sensing and communications: Toward dual-functional wireless networks for 6G and beyond," *IEEE J. Sel. Areas Commun.*, vol. 40, no. 6, pp. 1728–1767, Jun. 2022.
- [13] Z. Gao, *et al.*, "Integrated sensing and communication with mmWave massive MIMO: A compressed sampling perspective," *IEEE Trans. Wirel. Commun.*, vol. 22, no. 3, pp. 1745–1762, Mar. 2023.
- [14] F. Dong, *et al.*, "Joint beamforming design for dual-functional MIMO radar and communication systems guaranteeing physical layer security," *IEEE Trans. Green Commun. Netw.*, vol. 7, no. 1, pp. 537–549, Mar. 2023.
- [15] Y. Liu, I. Al-Nahhal, O. A. Dobre, F. Wang, and H. Shin, "Extreme learning machine-based channel estimation in IRS-Assisted multi-user ISAC system," *IEEE Trans. Commun.*, 2023, [early access].
- [16] A. Adhikary, M. S. Munir, A. D. Raha, Y. Qiao, Z. Han, and C. S. Hong, "Integrated sensing, localization, and communication in holographic MIMO-enabled wireless network: A deep learning approach," *IEEE Trans. Netw. Service Manag.*, 2023, [early access].
- [17] E. Shtawi, H. Zhang, A. Abdelhadi, A. L. Swindlehurst, Z. Han, and H. V. Poor, "Sum-rate maximization for RIS-assisted integrated sensing and communication systems With manifold optimization," *IEEE Trans. Commun.*, vol. 71, no. 8, pp. 4909–4923, Aug. 2023.
- [18] A. R. Chiriyath, B. Paul, and D. W. Bliss, "Radar-communications convergence: Coexistence, cooperation, and co-design," *IEEE Trans. Cogn. Commun. Netw.*, vol. 3, no. 1, pp. 1–12, Mar. 2017.
- [19] Z. Feng, *et al.*, "Joint radar and communication: A survey," *China Commun.*, vol. 17, no. 1, pp. 1–27, Jan. 2020.
- [20] W. Zhou, R. Zhang, G. Chen, and W. Wu, "Integrated sensing and communication waveform design: A survey," *IEEE Open J. Commun. Soc.*, vol. 3, pp. 1930–1949, Oct. 2022.
- [21] C. Sturm, T. Zwick, and W. Wiesbeck, "An OFDM system concept for joint radar and communications operations," in *Proc. VTC Spring 2009* (Barcelona, Spain), Apr. 26–29, 2009, pp. 1–5.
- [22] M. Braun, C. Sturm, and F. K. Jondral, "Maximum likelihood speed and distance estimation for OFDM radar," in *Proc. 2010 IEEE Radar Conf.* (Arlington, VA, USA), May 10–14, 2010, pp. 256–261.
- [23] A. Ghosh, *et al.*, "LTE-advanced: Next-generation wireless broadband technology," *IEEE Wirel. Commun.*, vol. 17, no. 3, pp. 10–22, Jun. 2010.
- [24] J. Yli-Kaakinen, *et al.*, "Frequency-domain signal processing for spectrally-enhanced CP-OFDM waveforms in 5G new radio," *IEEE Trans. Wirel. Commun.*, vol. 20, no. 10, pp. 6867–6883, Oct. 2021.
- [25] B. M. Popović, "Optimum sets of interference-free sequences with zero autocorrelation zones," *IEEE Trans. Inf. Theory*, vol. 64, no. 4, pp. 2876–2882, Apr. 2018.
- [26] R. Liu, *et al.*, "Integrated sensing and communication based outdoor multi-target detection, tracking and localization in practical 5G networks," *arXiv e-prints*, arXiv:2305.13924, May 2023.
- [27] S. Zhou, X. Liang, Y. Yu, and H. Liu, "Joint radar-communications co-use waveform design using optimized phase perturbation," *IEEE Trans. Aerosp. Electron. Syst.*, vol. 55, no. 3, pp. 1227–1240, Jun. 2019.
- [28] F. Dong, *et al.*, "Sensing as a service in 6G perceptive networks: A unified framework for ISAC resource allocation," *IEEE Trans. Wirel. Commun.*, vol. 22, no. 5, pp. 3522–3536, May 2023.
- [29] S. Chen, Z. Xiao, and Y. Zeng, "Simultaneous beam sweeping for multi-beam integrated sensing and communication," in *Proc. ICC 2022* (Seoul, South Korea), May 16–20, 2022, pp. 4438–4443.
- [30] M. Bică and V. Koivunen, "Multicarrier radar-communications waveform design for RF convergence and coexistence," in *Proc. ICASSP 2019* (Brighton, UK), May 12–17, 2019, pp. 7780–7784.
- [31] C. Shi, F. Wang, S. Salous, and J. Zhou, "Joint subcarrier assignment and power allocation strategy for integrated radar and communications system based on power minimization," *IEEE Sens. J.*, vol. 19, no. 23, pp. 11167–11179, Dec. 2019.
- [32] C. Shi, *et al.*, "Joint optimization scheme for subcarrier selection and power allocation in multicarrier dual-function radar-communication system," *IEEE Syst. J.*, vol. 15, no. 1, pp. 947–958, Mar. 2021.
- [33] X. Cao, *et al.*, "Robust OFDM shared waveform design and resource allocation for the integrated sensing and communication system," in *Proc. WCNC 2023* (Glasgow, UK), Mar. 26–29, 2023, pp. 1–6.
- [34] Y. Chen, *et al.*, "Joint subcarrier and power allocation for integrated OFDM waveform in RadCom systems," *IEEE Commun. Lett.*, vol. 27, no. 1, pp. 253–257, Jan. 2023.
- [35] Y. Ma, *et al.*, "Highly efficient waveform design and hybrid duplex for joint communication and sensing," *IEEE Internet Things J.*, vol. 10, no. 19, pp. 17369–17381, Oct. 2023.
- [36] R. W. Heath, *et al.*, "An overview of signal processing techniques for millimeter wave MIMO systems," *IEEE J. Sel. Topics Signal Process.*, vol. 10, no. 3, pp. 436–453, Apr. 2016.
- [37] H. Senol and C. Tepedelenlioglu, "Subspace-based estimation of rapidly varying mobile channels for OFDM systems," *IEEE Trans. Signal Process.*, vol. 69, pp. 385–400, 2021.
- [38] M. Kronauge and H. Rohling, "Fast two-dimensional CFAR procedure," *IEEE Trans. Aerosp. Electron. Syst.*, vol. 49, no. 3, pp. 1817–1823, Jul. 2013.
- [39] F. Zhang, T. Mao, and Z. Wang, "Doppler-resilient design of CAZAC sequences for mmWave/THz sensing applications," *IEEE Trans. Veh. Technol.*, 2023, [early access].
- [40] M. H. AlSharif, *et al.*, "Range estimation of a moving target using ultrasound differential Zadoff–Chu codes," *IEEE Trans. Instrum. Meas.*, vol. 70, article 8502415, pp. 1–15, Apr. 2021.
- [41] P. He, L. Zhao, S. Zhou, and Z. Niu, "Water-filling: A geometric approach and its application to solve generalized radio resource allocation problems," *IEEE Trans. Wirel. Commun.*, vol. 12, no. 7, pp. 3637–3647, Jul. 2013.
- [42] M. Grant, S. Boyd, and Y. Ye, "CVX: Matlab software for disciplined convex programming," <http://cvxr.com/cvx>, 2016.
- [43] E. Björnson, M. Matthaiou, and M. Debbah, "A new look at dual-hop relaying: Performance limits with hardware impairments," *IEEE Trans. Commun.*, vol. 61, no. 11, pp. 4512–4525, Nov. 2013.
- [44] F. Liu, *et al.*, "Toward dual-functional radar-communication systems: Optimal waveform design," *IEEE Trans. Signal Process.*, vol. 66, no. 16, pp. 4264–4279, Aug. 2018.
- [45] E. Chouzenoux and J.-C. Pesquet, "Convergence rate analysis of the majorize-minimize subspace algorithm," *IEEE Signal Process. Lett.*, vol. 23, no. 9, pp. 1284–1288, Sep. 2016.